

Direct observations of NO_x emissions over the San Joaquin Valley using airborne flux measurements during RECAP-CA 2021 field campaign

Qindan Zhu^{1,*}, Bryan Place^{2,**}, Eva Y. Pfannerstill³, Sha Tong^{4,5}, Huanxin Zhang⁴, Jun Wang⁴, Clara M. Nussbaumer^{1,6}, Paul Wooldridge², Benjamin C. Schulze⁷, Caleb Arata⁸, Anthony Bucholtz⁹, John H. Seinfeld⁷, Allen H. Goldstein^{3,8}, and Ronald C. Cohen^{1,2}

¹Department of Earth and Planetary Sciences, University of California, Berkeley, Berkeley, CA 94720, United States

*Now at Department of Earth, Atmospheric and Planetary Sciences, Massachusetts Institute of Technology, Cambridge, MA, United States of America

²Department of Chemistry, University of California, Berkeley, Berkeley, CA 94720, United States

**Now at Office of Research and Development, U.S. Environmental Protection Agency, Research Triangle Park, North Carolina 27711, United States

³Department of Environmental Science, Policy, and Management, University of California, Berkeley, Berkeley, CA 94720, United States

⁴Department of Chemical and Biochemical Engineering, Center for Global and Regional Environmental Research, and Iowa Technology Institute, University of Iowa, Iowa City, Iowa 52242, United States

⁵Collaborative Innovation Center on Forecast and Evaluation of Meteorological Disasters (CIC-FEMD), Key Laboratory for Aerosol-Cloud-Precipitation of China Meteorological Administration, Nanjing University of Information Science Technology, Nanjing 210044, People's Republic of China

⁶Department of Atmospheric Chemistry, Max Planck Institute for Chemistry, Mainz 55128, Germany

⁷Department of Environmental Science and Engineering, California Institute of Technology, Pasadena, CA 91125, United States

⁸Department of Civil and Environmental Engineering, University of California, Berkeley, Berkeley, CA 94720, United States

⁹Department of Meteorology, Naval Postgraduate School, Monterey, CA 93943, United States

Correspondence: Qindan Zhu (qindan_zhu@berkeley.edu) and Ronald C. Cohen (rccohen@berkeley.edu)

Abstract. Nitrogen oxides (NO_x) are principle components of air pollution and serve as important ozone precursors. As the San Joaquin Valley (SJV) experiences some of the worst air quality in the United States, reducing NO_x emissions is a pressing need, yet quantifying current emissions is complicated due to a mixture of mobile and agriculture sources. We performed airborne eddy covariance flux measurements during the Re-Evaluating the Chemistry of Air Pollutants in CALifornia (RECAP-CA) field campaign in June 2021. Combining footprint calculations and land cover statistics, we disaggregate the observed fluxes into component fluxes characterized by three different land cover types. On average we find emissions of **2.95 mg 0.95 mg N** m⁻² h⁻¹ over highways, **1.24 mg 0.43 mg N** m⁻² h⁻¹ over urban areas and **0.79 mg 0.30 mg N** m⁻² h⁻¹ over croplands. The calculated NO_x emissions using flux observations are utilized to evaluate anthropogenic emission inventories and soil NO_x emission schemes. We show that two anthropogenic inventories for mobile sources, EMFAC (EMission FACtor) and FIVE (Fuel-based Inventory for Vehicle Emissions), yield **similar strong** agreement with emissions derived from measured fluxes over urban regions **with 24% and 22% low bias, respectively**. Three soil NO_x schemes, including MEGAN v3 (Model of Emissions of Gases and Aerosols from Nature), BEIS v3.14 (Biogenic Emission Inventory System) and BDISNP (Berkeley

Dalhousie Iowa Soil NO Parameterization), show substantial underestimates over the study domain. Compared to the cultivated soil NO_x emissions derived from measured fluxes, MEGAN and BEIS are lower by more than one order of magnitude and BDISNP is lower by a factor of 2.72.2. Despite the low bias, observed soil NO_x emissions and BDISNP present a similar spatial pattern as well as temperature dependence. We conclude that soil NO_x is a key feature of the NO_x emissions in the SJV and that a ~~state-of-the-science~~ biogeochemical process-based model of these emissions is needed to simulate emissions for modeling air quality in the region.

1 Introduction

20 Nitrogen oxides (NO_x ≡ NO + NO₂) are important trace gases that affect both the gas and aerosol phases of tropospheric chemistry. NO_x regulates the concentrations of the primary atmospheric oxidant, hydroxyl radicals (OH), and serves as the catalyst for the formation of ozone (O₃). NO_x also affects the formation of inorganic nitrate aerosol through the production of nitric acid (HNO₃) and organic nitrates (RONO₂) and plays a role in secondary organic aerosol (SOA) production. NO_x, O₃ and aerosol are all detrimental to human health, triggering respiratory diseases (Kampa and Castanas, 2008; Hakeem et al., 25 2016) and leading to premature death (Lelieveld et al., 2015).

NO_x is predominantly emitted from anthropogenic sources, including light and heavy-duty transportation, fuel combustion, and biomass burning. Among these sectors transportation is the largest in the United States (EPA, 2016). Strict regulations have been implemented to control NO_x emissions. Three-way catalysts have effectively reduced emissions from gasoline-powered passenger vehicles. The application of emission control systems on coal power plants has reduced NO_x emissions 30 (De Gouw et al., 2014). The California Air Resources Board (CARB) has proposed Heavy-Duty Engine and Vehicle Omnibus Regulation and Associated Amendments and target for 90% reduction in per-vehicle heavy-duty NO_x emission by 2031 (CARB, 2016). The regulation of mobile sources leads to an increasing importance of natural NO_x sources, such as lightning and soil emissions. Soil NO_x is released as a byproduct of microbial nitrification and denitrification (Andreae and Schimel, 1990). While the biogeochemistry of soil NO_x emission is well established, this biogenic source involves a complex interaction of 35 soil microbial activity, soil nitrogen (N) content. Besides, agriculture activities, such as the use of fertilizers, lead to a substantial enhancement of soil NO_x emissions (Phoenix et al., 2006).

Currently, the San Joaquin Valley (SJV) in California experiences some of the most severe air pollution in the United States. The SJV cities, Visalia, Fresno, and Bakersfield are among the top ten most polluted cities for both ozone and particulate matter (American Lung Association, 2020). In order to implement appropriate emission control efforts, identifying the contribution 40 of different NO_x emissions are particularly important for the SJV as it features a complex mixture of emissions from fuel combustion and soil emissions associated with agriculture. The contribution of soil NO_x emissions remains highly uncertain. While Guo et al. (2020) attribute approximately 1.1% of anthropogenic NO_x emissions in California to soil NO_x, Almaraz et al. (2018) argued that due to growing N fertilizer use, the SJV has soil NO_x emissions of 24 kg of N ha⁻¹ year⁻¹, contributing 20-51% of the NO_x budget of the entire state of California. ~~In contrast, Guo et al. (2020) attribute approximately 1.1% of~~

45 ~~anthropogenic emissions in California to soil~~ Similarly, [Sha et al. \(2021\)](#) estimated that 40.1% of the total NO_x emissions over California in July 2018 are from soils.

Airborne eddy covariance (EC) flux measurements provide a powerful tool to investigate the emission strength of atmospheric constituents at landscape scales. It has been applied to assess the surface exchanges of greenhouse houses (GHGs) including CO₂ and methane (CH₄) (Mauder et al., 2007; Yuan et al., 2015; Sayres et al., 2017; Hannun et al., 2020). In recent 50 years it has been extended to study emissions of volatile organic compounds and NO_x over a megacity (Karl et al., 2009; Vaughan et al., 2021), vegetation (Karl et al., 2013; Misztal et al., 2014; Wolfe et al., 2015; Kaser et al., 2015; Yu et al., 2017; Gu et al., 2017), and shale gas production regions (Yuan et al., 2015). Compared to the traditional EC measurements from instruments mounted at a fixed location on a tower, wavelet-based airborne EC measurements allow for larger spatial assessment and are well suited to regions with inhomogeneous and non-stationary source distributions (Sührling et al., 2019).

55 In this study, we present airborne EC flux measurements obtained during seven flights of a Twin Otter aircraft over the San Joaquin Valley in California. Companion studies of NO_x emissions over Los Angeles (~~Nussbaumer et al. 2022, submitted~~) and VOC (~~Pfannerstill et al. in prep~~) ([Nussbaumer et al., 2023](#)) and VOC ([Pfannerstill et al., 2023](#)) and GHG fluxes (Schulze et al. in prep) will be presented separately. We utilize continuous wavelet transformation to calculate the NO_x flux (Sect. 3). In conjunction with footprint calculations and land classification, we explore the spatial heterogeneity of NO_x emissions and 60 identify component fluxes from the highway, urban, and soil land types (Sect. 4). We also utilize the NO_x emissions derived from flux measurements to evaluate anthropogenic emission inventories and soil NO_x schemes (Sect. 5).

2 Measurements

The airborne EC flux measurements were conducted on a Twin Otter research aircraft operated by the Naval Postgraduate School (NPS) during the Re-Evaluating the Chemistry of Air Pollutants in CALifornia (RECAP-CA) field campaign. The 65 RECAP-CA field campaign was conducted between June 1st to June 22nd in California, including 7 days of measurements over the San Joaquin Valley and 9 days of measurements over Los Angeles. The flight path was designed with long straight legs to ensure good quality of flux measurements (Figure S1) (Karl et al., 2013). The aircraft flew slowly, at the airspeed of 50-60 m/s, and cruised at a low height of ~ 300 m above ground. The aircraft took off at ~11:00 local time at Burbank Airport and landed at ~18:00 local time.

70 The standard instruments aboard the aircraft are described in (Karl et al., 2013) and include total and dew point temperature, barometric and dynamic pressures, wind direction and wind speed, total airspeed, slip- and attack angles, GPS latitude, GPS longitude, GPS altitude, pitch, roll, and heading. These measurements are at ~~10Hz~~ 10 Hz temporal resolution.

VOCs were measured at 10 Hz time resolution by Vocus proton transfer reaction time of flight mass spectrometer (Vocus PTR-ToF-MS) as described in Pfannerstill et al. (2023). Mixing ratios of NO_x were measured at 5 Hz frequency using a 75 ~~three-channel~~ custom-built three-channel thermal dissociation-laser induced fluorescence (TD-LIF) instrument. ~~Ambient air was sampled~~ The multipass LIF cells, fluorescence collection, long-pass wavelength filtering (for $\lambda > 700$ nm), and photon

counting details have been previously described (Thornton et al., 2000; Day et al., 2002; Wooldridge et al., 2010). Details specific to this implementation are described below.

Air was sampled from the aircraft community inlet through PFA Teflon tubing at a rate of ~ 6 L/min and the sample flow was split equally between the three instrument channels. The first channel provided measurements of Each measured NO_2 via the laser-induced fluorescence of molecules with utilizing a compact green laser (Spectra-Physics ExplorerOneXP 532 nm). The laser was pulsed at 80 kHz and the 1.7 Watt average power was split between the three cells. An excess flow of was introduced into the second channel to provide measurements of total by converting all NO in the sample flow to Earlier versions of the instrument used a dye laser tuned on and off a narrow rovibronic NO_2 before detection. The red-shifted fluorescence from the molecules was collected, wavelength filtered and quantified with time-gated photon counting modules (Hamamatsu H7421-50). The third TD-LIF channel was used to measure the sum of all other higher nitrogen oxides (NO_x) by thermally dissociating to with an inline oven (~ 500 C) before LIF detection. All three detection cells were maintained resonance at 585.1 nm. Experience over a wide variety of conditions had demonstrated the off-line signal did not depend on the sample, other than from aerosol particles and that could be eliminated by adding a Teflon membrane filter. Moving to nonresonant excitation at 532 nm provided full-time coverage at 5 Hz along with lower complexity and more robust performance of the laser system. Maintaining the LIF cells at low pressure (~ 0.4 kPa) was no longer required to avoid line-broadening but was still desirable to minimize collisional quenching of the molecules and to extend the fluorescence lifetime so the observing gate can be limited to the time after the laser pulse. Instrument NO_2 fluorescence lifetime for time-gated photon counting to reject prompt laser scatter. Instrument zeros were run using ambient air scrubbed of NO_x every 20 minutes in flight to correct for any background drift during the flights. In addition, calibrations were performed in-flight every 60 minutes using a standardized NO_2 in N_2 calibration cylinder (Praxair, 5.5 ppm, Certified Standard grade) diluted with scrubbed air. In addition, instrument zeros were run using ambient air scrubbed of all reactive gases every 20 minutes in flight to correct for any background drift during the flights. A more complete description of

NO_2 was measured directly in the first channel, with the sample passing only through a particle filter and a flow-limiting orifice before the cell. NO_x was measured in the TD-LIF instrument specifics and analytical performance can be found in previous literature (Thornton et al., 2000; Day et al., 2002; Wooldridge et al., 2010) second by adding O_3 (generated with 184.5 nm light and a flow of scrubbed and dried air) to convert NO to NO_2 before detection. A 122 cm length of 0.4 cm i.d. tubing served as the O_3 +NO reactor, providing 4 seconds of reaction time before the orifice. The third channel was used to measure the sum of higher nitrogen oxides (e.g. organic nitrates and nitric acid) by thermal dissociation to NO_2 with an inline oven (~ 500 C) before LIF detection.

3 Flux and footprint calculation

3.1 Pre-processing

The observed 10 Hz vertical wind speeds are downscaled to 5 Hz in order to match the time resolution of NO_x measurements. The full observation data set breaks into segments with continuous wind and NO_x measurements. The segment window is

110 selected if the length is larger than 10 km and the height variation is less than 200 m. We also filter out measurements when aircraft roll angles are larger than 8 degrees to avoid perturbation in the vertical wind due to aircraft activity. While most of the measurements are within the ~~boundary layer~~planetary boundary layer (PBL), the airplane arose above the boundary layer occasionally. ~~We obtain the hourly boundary layer height and these observations above PBL are removed in later analysis.~~
 115 The PBL heights are determined using the sharp gradient in the dew point, water concentration, toluene concentration and temperature at the soundings conducted during the voyage, and we interpolate the PBL heights to the full duration of the flight.
The PBL heights agree well against the hourly PBL heights from the High-Resolution Rapid Refresh (HRRR) product ~~at the spatial resolution of 3 km. The observations are removed if the aircraft exceeds the planetary boundary layer (PBL) height from HRRR~~(Figure. S2).

We adjust for the lag time between the meteorology measurements and the TD-LIF measurements by shifting the time of
 120 TD-LIF observation within the time window of ± 4 seconds until the covariance with the vertical wind speed is maximized (Figure. S4). As the time lag is assumed to be due to differences in the clocks of the two instruments and the transit time of air through the TD-LIF instrument, we assume that the lag time for each flight is constant. We use the median lag time from each flight for all segments collected on the same day.

3.2 Continuous wavelet transformation

125 The continuous wavelet transformation (CWT) parameterization decomposes the time series ($x(t)$) into a range of frequencies and represents it as the convolution of the time series with a wavelet function ([Torrence and Compo, 1998](#)).

$$W(a, b) = \int_{-\infty}^{\infty} x(t) \psi_{a,b}^*(t) dt \quad (1)$$

$$\psi_{a,b}^*(t) = \frac{1}{\sqrt{a}} \psi_0\left(\frac{t-b}{a}\right) \quad (2)$$

where $W(a, b)$ is the wavelet coefficient; $\psi_{a,b}^*(t)$ is the wavelet function, which is based on a “mother” wavelet ψ_0 and is
 130 adjusted with a transition parameter b and a scale parameter a . The transition parameter determines the location of the “mother” wavelet and the scale parameter defines the frequency. We use the Morlet wavelet as the “mother” wavelet.

$$\psi_0 = \pi^{-1/4} e^{6i\eta} e^{-\eta^2/2} \quad (3)$$

The Morlet wavelet has been widely applied to represent turbulence in the atmosphere due to a reasonable localization in the frequency domain and a good ability of edge detection (Schaller et al., 2017).

135 Time domain scales are increased linearly with the increment of the time resolution ($\delta t, 0.2s$), and ~~frequency~~N is the number of data points. Frequency domain scales are represented by an exponential array of scale parameters a_j with the increment δj of 0.25s. The ~~largest~~smallest frequency scale is the Nyquist frequency, which is twice the time resolution (0.4s).

$$b_n = \underline{n}N\delta t \quad (4)$$

$$a_j = a_0 \times 2^{j\delta j} \quad (5)$$

140 For two simultaneous time series of NO_x ($W_c(a, b)$) and vertical wind speed ($W_w(a, b)$), we first detrend them by subtracting out the average followed by dividing the standard deviation of a scalar time series. Then we obtain the wavelet cross-spectrum (following Eqn. 9). The Morlet wavelet-specific reconstruction factor C_δ is 0.776. We then sum up over the full frequency scales to yield a time series of flux (Eqn. 10).

$$\bar{W}_c = \frac{1}{N} \sum_{i=1}^N W_{ci} \quad \text{and} \quad \bar{W}_w = \frac{1}{N} \sum_{i=1}^N W_{wi} \quad (6)$$

$$145 \quad \hat{\sigma}_c^2 = \frac{1}{N-1} \sum_{i=1}^N (W_{ci} - \bar{W}_c)^2 \quad \text{and} \quad \hat{\sigma}_w^2 = \frac{1}{N-1} \sum_{i=1}^N (W_{wi} - \bar{W}_w)^2 \quad (7)$$

$$\underline{W'_c(a, b)} = \frac{(W_c(a, b) - \bar{W}_c)}{\hat{\sigma}_c} \quad \text{and} \quad \underline{W'_w(a, b)} = \frac{(W_w(a, b) - \bar{W}_w)}{\hat{\sigma}_w} \quad (8)$$

$$E_{c,w}(j) = \frac{\delta t}{C_\delta} \frac{1}{N} \sum_{n=0}^{N-1} [W'_c(a, b) \cdot W'_w{}^*(a, b)] \quad (9)$$

$$F(t) = \hat{\sigma}_c \hat{\sigma}_w \overline{c'w'} = \hat{\sigma}_c \hat{\sigma}_w \frac{\delta t}{C_\delta} \frac{\delta j}{N} \sum_{n=0}^{N-1} \sum_{j=0}^J \frac{[W_c(a, b) \cdot W_w^*(a, b)]}{a(j)} \frac{[W'_c(a, b) \cdot W'_w{}^*(a, b)]}{a(j)} \quad (10)$$

Figure 1 exhibits an example of CWT flux calculation. Figure 1 (a) shows the detrended NO_x and vertical wind speed in a straight segment of ~ 50 km. The detrending is realized by subtracting out the average followed by dividing the standard deviation of a scalar time series. Both time series are decomposed using CWT algorithm to yield the cross-power spectrum shown in Figure 1 (b). Due to the finite length in time, the wavelet power spectrum is prone to higher uncertainties closer to the edge (Mauder et al., 2007). The regions of the wavelet power spectrum where the edge effects are the largest are identified as the Cone of Influence (COI). Data points containing $>80\%$ spectral power within the cone of influence are removed for quality control. The power spectrum is then integrated over all frequencies to the time series of NO_x flux (Figure 1 (c)). ~~To address the influence of large-scale turbulence, we~~ We processed the integrated fluxes as 2 km moving averages ~~and to address the influence of large-scale turbulence and then~~ re-sampled them at 500 m.

3.3 Footprint calculation

The footprint describes the contribution of surface regions to the observed airborne flux. We use the KL04-2D parameterization to calculate a space-resolved footprint map. This KL04-2D parameterization is developed from a 1-D backward Lagrangian stochastic particle dispersion model (Kljun et al., 2004). Metzger et al. (2012) implemented a Gaussian cross-wind distribution function to resolve the dispersion perpendicular to the main wind direction. The input parameters include the height of the measurements, standard deviation of horizontal and vertical wind speed, horizontal wind direction, boundary layer height, surface roughness length, and friction velocity. We obtain the ~~boundary layer height and~~ surface roughness length and friction velocity from the HRRR product. ~~The friction velocity is inferred using the logarithmic wind profile given the observed horizontal wind speed, measurement height, and surface roughness length (Högström, 1988).~~

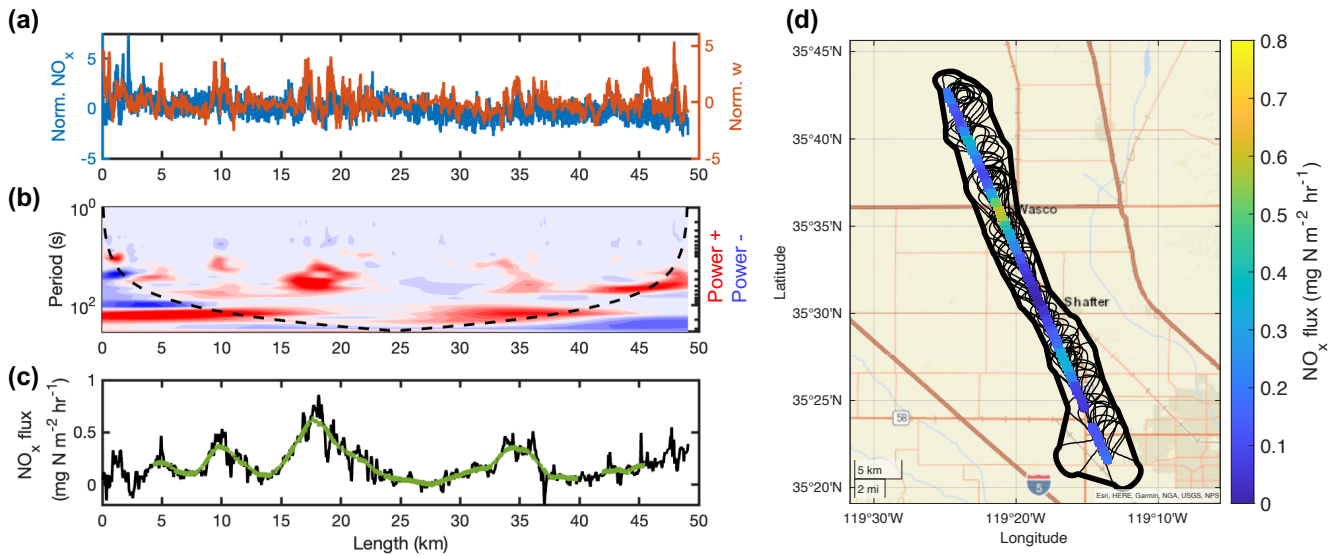


Figure 1. a) The variance of NO_x and vertical wind speed, b) frequency and time-resolved wavelet power spectrum with the cone of influence shown as a black dotted line, c) the integrated fluxes from the raw data points are shown in black, the fluxes after moving averaging and COI filtering are shown in green. The dashed gray line indicates the detection limit of this segment. d) the distribution map of flux re-sampled at 500m. The gray-black lines show the 9th-90th percentiles of the footprints and the thick black line denotes the contours of all footprints.

For each flux observation, we calculate the footprint map at the spatial resolution of 500m and then extract the 90% contour. Figure 1 (d) depicts the 90% KL04-2D footprint contours of observations resampled to 500 m in one segment. Each footprint contour is aligned with the horizontal wind direction and is transformed into a geographic coordinate space.

170 3.4 Filter out NO_x fluxes impacted by the off-road vehicle emissions

175 It is worth noting that croplands includes not only soil NO_x emissions but the off-road vehicle emissions. Erroneously attributing the NO_x from off-road vehicle emissions to soil NO_x emissions leads to a high bias. While trimethylbenzene was observed during RECAP-CA field campaign, Pfannerstill et al. (2023) presented the trimethylbenzene fluxed using the same algorithm described in Sect.3.2. The trimethylbenzene fluxes are interpolated to match the NO_x fluxes in time and are utilized as an indicator of off-road vehicle emissions over croplands (Tsai et al., 2014). The trimethylbenzene fluxes are categorized into two groups; the first group presents footprints covering croplands exclusively and the second group presents footprints with mixed land cover types. Shown in Figure S9, the trimethylbenzene flux is much lower over croplands, a median of $0.003 \text{ mg m}^{-2} \text{ h}^{-1}$ compared to a median of $0.009 \text{ mg m}^{-2} \text{ h}^{-1}$ over mixed land cover types including highway and urban areas. Among all observations over cropland, we identify those with the trimethylbenzene flux larger than $0.02 \text{ mg m}^{-2} \text{ h}^{-1}$, which consists of 7% of the total data points, are impacted by the off-road vehicle emissions, and then filter out them in the later analysis. We

180

also vary the threshold of the trimethylbenzene flux between 0.005 mg m⁻² h⁻¹ and 0.04 mg m⁻² h⁻¹ and conclude that the choice of the threshold does not influence the results.

3.5 Vertical divergence

185 Extrapolating the airborne flux to surface flux should account for the vertical divergence. The vertical divergence is a result of multiple processes, including net in-situ production or loss, storage, and horizontal advection.

To investigate the impact of vertical divergence, the flight route includes three vertically stacked racetracks, during which the segments are close to each other in space but vary in height. After removing the legs that fail the quality control, only one racetrack measurement carried out between 14:20 to 15:10 on June 8th presented qualified flux segments, and the vertical distribution of fluxes is shown in Fig. S4. No consistent increase or decrease of fluxes with increasing height is detected during
190 the racetrack in this study because the vertical divergence is hampered by emission heterogeneity. Shown in Fig. S7, the footprint map for each segment at various altitudes covers regions with high heterogeneity. Therefore, we use an alternative approach to calculate the vertical divergence. Instead of extracting racetrack measurements, we collect a subset of flux measurements during the whole field campaign based on the footprint coverage. Only fluxes with footprints covering croplands exclusively are included to avoid emission heterogeneity. We use PBL height (z_i) from HRRR to calculate the ratio of measurement heights relative to the PBL height (z/z_i) and 98% of selected fluxes are located within 70% of the PBL height and they are divided into 7 bins of z/z_i with uniform width. We then perform a linear fit for the binned median fluxes versus z/z_i and use the regression result to calculate the linearly extrapolated surface fluxes. vertical correction factor ($C = \frac{\text{slope}}{\text{intercept}}$). This correction factor is used to linearly extrapolated the fluxes at the measurement height (F_z) to fluxes at the surface (F_0) (Eqn. 11). After vertical divergence correction, the surface fluxes are on average 3026% higher than the fluxes at the measurement
200 heights.

$$F_0 = \frac{F_x}{1 + C \frac{z}{z_i}} \quad (11)$$

3.6 ~~Uncertainty~~ Data quality control and uncertainty analysis ~~The flux-~~

The flux detection limit does not only depend on the signal-to-noise ratio of the NO_x measurement, but also varies with wind speed and atmospheric stability. Following Langford et al. (2015), we calculate the detection limit of flux (LoD) before the moving and spatial average are applied. For each segment, the observed NO_x is replaced with a white noise time series and is then feed into the CWT to yield the corresponding time series of “noise” flux. The random error affecting the flux ($\sigma_{NO_x, noise}$) is defined as the standard deviation of this noise-derived flux, and LoD is defined as $2 \times \sigma_{NO_x, noise}$ (95th confidence level). Among 142 segments, Figure 3 (a) shows the distribution of flux LoD among 142 segments. The LoDs range from 0.02 mg N m⁻² h⁻¹ to 0.30 mg N m⁻² h⁻¹, and the average LoD is 0.10 mg N m⁻² h⁻¹. To obtain a better constraint on the flux quality,

205

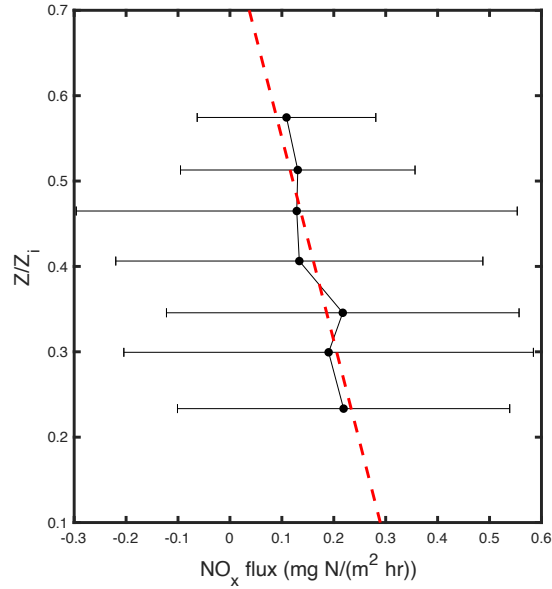


Figure 2. Vertical profiles of measured fluxes above croplands during RECAP-CA field campaign binned by the ratio of measurement height and PBL height (z/z_i). The points represent the median flux within each bin, and the error bars represent the standard deviation. The red dashed line shows a linear fit for median fluxes versus relative height.

210 we compare the LoD against the time series of flux in each segment and filter out 18 segments in which the whole time series is below the LoD.

The flux calculation using CWT introduces uncertainty from a variety of sources. We describe systematic errors and random errors following Wolfe et al. (2018).

215 Systematic errors arise from the under-sampling of high-frequency and low-frequency ranges. The CWT algorithm fails to resolve a frequency higher than the Nyquist frequency. Due to the high temporal resolution ~~of data points~~ (5 Hz), we expect a minimal loss ~~of at the~~ high-frequency limit (Figure. S5). The upper limit of systematic error associated with low frequency is calculated using Eqn. 12 (Lenschow et al., 1994).

$$SE \leq 2.2 \left(\frac{z}{z_i} \right)^{0.5} \frac{z_i}{L} \quad (12)$$

z and L are the measurement heights and the length of segments, respectively. z_i are the boundary layer heights from HRRR.

220 We calculate the low-frequency error ranges from 1%-5%.

Random errors ~~define the detection limit of the CWT. The detection limit is assessed by assigning a randomly generated wind speed of a unity standard deviation and recalculating flux using this random wind speed series and observed mixing ratio. The fractional uncertainty is determined by using 3× standard deviation of the detection limit divided by the average flux for each segment, yielding a mean fractional error of 52% after averaging to 2 km.~~ arise from the noise in the instrument (RE_{noise}) as

225 well as the noise in turbulence sampling (RE_{turb}), which are calculated using Eqn. 13 and Eqn. 14 (Wolfe et al., 2018; Lenschow et al., 199

$$RE_{noise} = \frac{\sqrt{\sigma_{NO_x, noise}^2 \sigma_w^2}}{N} \quad (13)$$

$$\frac{RE_{turb}}{F} \leq 1.75 \left(\frac{z}{z_i}\right)^{0.25} \left(\frac{z_i}{L}\right)^{0.5} \quad (14)$$

230 z , L and z_i are the same as Eqn. 12, σ_w^2 is the variance of vertical wind speed. Note that RE_{noise} assumes the noise in each time step is uncorrelated, therefore, we ignore the moving average step in the uncertainty calculation and N denotes the number of points used to yield each 500m spatially averaged flux.

Utilizing a constant lag time introduces an additional source of uncertainty. We estimate the uncertainty by comparing the calculated fluxes using segment-specific and constant lag times across all segments that specific lag times are available. Shown in Figure. S4, the difference is less than 25% for 90 percent of the data. Therefore, we attribute an uncertainty of 25% due to the lag time correction (RE_{lag}). While we believe this error is unphysical and that a single lag time is more appropriate, we include it to be conservative in our estimate of the uncertainties.

240 Estimating the uncertainty caused by the correction of vertical divergence is tricky. While we conclude that the influence of vertical divergence is non-negligible, it is ignored in some previous airborne flux studies (e.g. Vaughan et al., 2016; Hannun et al., 2020; Vaughan et al., 2021; Drysdale et al., 2022). ~~Here we only consider the uncertainty of 20% associated with the linear regression results in the vertical divergence correction. However, the uncertainty is arguably higher and is yet challenging to quantify as~~ While the flux is scattered in each vertical intervals in our divergence calculation, we first bootstrap the flux observations and calculate the uncertainty of correction factor (σ_C) to 40%. As we see a significant difference in vertical correction factor on racetrack measurements versus a selected subset of flux observations, ~~we tentatively set the uncertainty of C to 100%~~, in order to account for the case of no vertical divergence. Besides, we account for a 30% uncertainty in the PBL heights.

~~We treat each uncertainty component as independent and calculate the~~

245 We propagate the total uncertainty from each component using Eqn. 16 and the distribution of total uncertainty is shown in Figure 3 (b). The average uncertainty is 60% and the interquartile of total uncertainty ~~to be 40% and 78%~~ are 48% and 68%. The random error ~~in the CWT algorithm dominates~~ and the vertical divergence correction dominate the uncertainty and the uncertainty is consistent with previous studies (Wolfe et al., 2018; Vaughan et al., 2016).

$$\sigma_{F_z} = \sqrt{SE^2 + RE_{noise}^2 + RE_{turb}^2 + RE_{lag}^2} \quad (15)$$

$$\sigma_{F_0} = \sqrt{\frac{\sigma_{F_z}^2}{(1 + C \frac{z}{z_i})^2} + \sigma_C^2 \left(\frac{z}{z_i}\right)^2 \left(\frac{F_z}{(1 + C \frac{z}{z_i})}\right)^2 + \sigma_{z_i}^2 \left(\frac{Cz}{z_i^2}\right)^2 \left(\frac{F_z}{(1 + C \frac{z}{z_i})}\right)^2} \quad (16)$$

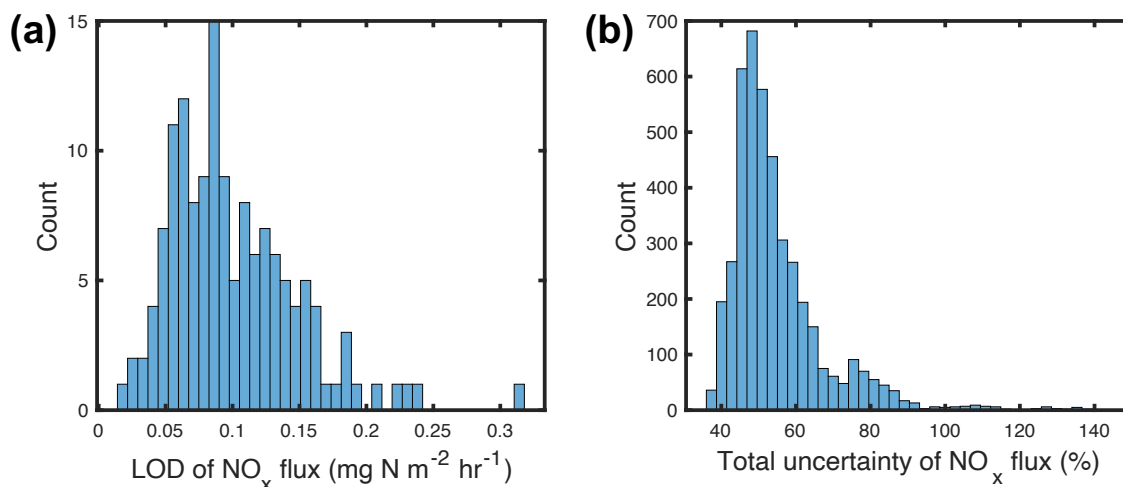


Figure 3. [a\) The distribution of segment-based \$\text{NO}_x\$ flux detection limit \(LoD\).](#) [b\) The distribution of total uncertainty of \$\text{NO}_x\$ flux.](#)

4 Component flux disaggregation

The overview of observed fluxes across 7 flights over San Joaquin Valley is illustrated in Fig. 4. It shows a distinct spatial
 255 heterogeneity (Figure 4 (a)). For instance, high NO_x flux signals are detected when the aircraft was flying above highway
 99 between Bakersfield and Visalia. The transect of cities, such as Fresno, capture a substantial enhancement of NO_x fluxes.
 Figure 4 (b) exhibits the [count-density distribution](#) of airborne fluxes. [8890%](#) of the fluxes are positive, demonstrating that our
 airborne flux measurements are capable of detecting NO_x emissions over the study domain. We attribute the remaining [1210%](#)
 of negative fluxes to the uncertainties in [calculation-including-an-incomplete-sampling-of-the-full-spectrum-of-eddies-the-flux](#)
 260 [calculation](#). The distribution of observed fluxes is right-skewed; the mean and median observed flux over the SJV is [1.01 mg](#)
[0.37 mg N m⁻² h⁻¹](#) and [0.65 mg-0.25 mg N m⁻² h⁻¹](#), respectively. The interquartile range of flux is [0.27 mg-0.11 mg N m⁻²](#)
[h⁻¹](#) and [1.38 mg-0.49 mg N m⁻² h⁻¹](#). [0.61, 2%](#) of extremely high fluxes exceeding [8 mg-2 mg N m⁻² h⁻¹](#) represents the long
 tail in the flux distribution, which are, like the negative fluxes, most likely caused by the incomplete sampling of the spectrum
 of eddies driving the fluxes.

265 As discussed in Sect. 3.3, we then calculate the footprint for each flux observation during the RECAP field campaign. Figure
 4 (a) shows the 90% footprint extent in grey. Fig. S8 shows that the 90% extent for the calculated footprints ranges from [0.25](#)
[to 11.7-0.16 to 12](#) km with a mean extent of [2.6-2.8](#) km. The KL04-2D footprint algorithm has been applied to airborne flux
 analysis over London and in that study, the 90% footprint extents range from 3 km to 12 km from the measurement (Vaughan
 et al., 2021). While the largest footprint extent is comparable with those from Vaughan et al. (2021), our calculated footprints
 270 mostly have a smaller extent as [7062%](#) of the footprint extents are within 3 km of the aircraft flight track. We attribute the
 small footprints to the stagnant weather conditions and weaker horizontal wind advection compared to London. The mean
 wind speed is 2.9 m/s for full observation data sets and 2.4 m/s for those data points with footprint extents less than 3 km.

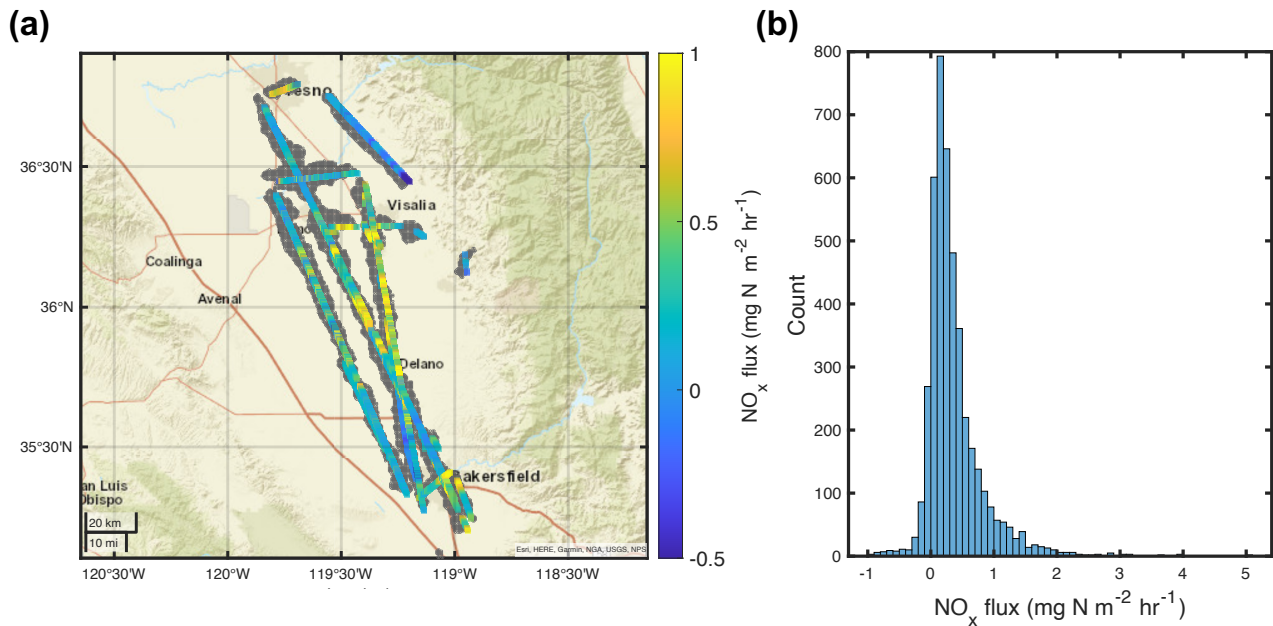


Figure 4. a) The map of observed airborne fluxes over 7 flights over the San Joaquin Valley. If the segment overlaps each other, the average flux is calculated. The grey shade represents the coverage of 90% footprint extents for all flux observations. b) The count density distribution of full data sets of observed airborne NO_x fluxes.

The largest footprint extent corresponds to observations at the foothills, due to higher altitude above the ground relative to the boundary layer height and stronger horizontal wind advection.

275 The region covered by the footprints is composed of mixed land cover types. We use the 2018 USDA CropScape database (<https://nassgeodata.gmu.edu/CropScape/>) to describe the land cover types. The resolution has been degraded from the native 30m resolution to 500m. For each grid, the land cover type is assigned if a land type makes up more than 50% of the 500m grid cell. We generalize a “soil” land cover type if the land cover type is identified as either cropland or grassland. The grids classified as “developed” in CropScape are dominated by anthropogenic activities including transportation and fuel combustion. We overlay the national highway network and categorize the grids containing highways as “highway” land types. The remaining grids are classified as “urban” and they correspond to the area with heavy populations in the absence of highways. The distinction between “highway” and “urban” land type is utilized to address on-road mobile sources. 2837% of the flux observations include the highway land type in the 90% footprint extent, 1523% of the observations include the urban land type and 9496% of the observations include cultivated soil land type.

285 To disentangle the flux emanating from different land cover types, we apply the Disaggregation combining Footprint analysis and Multivariate Regression (DFMR) methodology described in Hutjes et al. (2010). The observed fluxes are treated as the weighted sum of component fluxes from each land cover type:

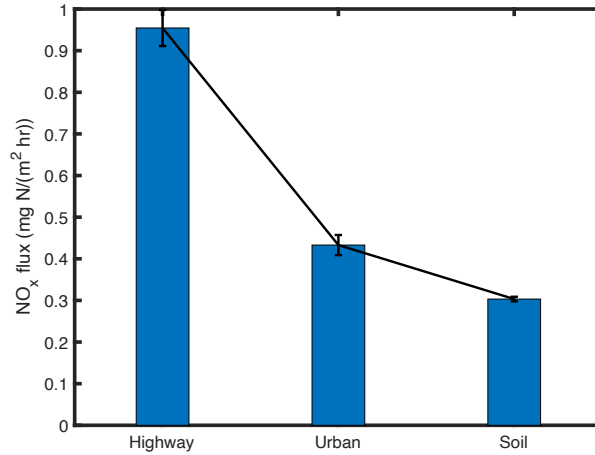


Figure 5. Bootstrapped statistical results of multi-linear regression to resolve component fluxes from the highway, urban, and cultivated soil land types. Each bar represents the average component fluxes from each land type and the black line shows the standard deviation.

$$F_{obs} = \sum_{k=1}^3 w_k F_k \quad (17)$$

where k_1 to k_3 denote highway, urban, and soil land types, w_k is the fractional area within the 90% footprint contour and F_k are the corresponding component fluxes from highway, urban, and soil land types, respectively. The multi-linear regression is applied to observations from all flights, consisting of 4749-4391 data points. To better quantify the uncertainty, we bootstrap the data samples and re-calculate the We perform the Monte Carlo simulation to identify the uncertainty of the multi-linear regression 100 times due to the flux uncertainty. The resulting statistical uncertainty is shown in Fig.5. The highway land type yields the highest flux of 2.95-0.96 mg N m⁻² h⁻¹ with a standard deviation of 0.14-0.04 mg N m⁻² h⁻¹. The areas classified as urban land type exhibit a flux of 1.24-0.43 (±0.10) mg N m⁻² h⁻¹, which is ~ 50% of the highway flux. Most likely the fluxes from highway are even higher than 2.95-0.96 mg N m⁻² h⁻¹. Note that the land type map is at 500m spatial scale, the grid classified as highway indeed includes both highway and areas near the highway. If, for example, the highway is only 10% of the true area of the land cover pixel, then the fluxes on the highway could be as much as 10 times larger. The cultivated soil land type flux of 0.79-0.30 (±0.02) mg N m⁻² h⁻¹ is large. It is about 1/4 the magnitude of the highway flux and half that of the urban flux. As the total area of soil pixels are much larger than the area of highway or urban pixels, integrated across the SJV, cultivated soil NO_x emissions are a major factor.

5 Calculation of NO_x emission map using airborne NO_x fluxes

While these separate component fluxes emphasize the distinction between individual land types at the spatial resolution of the ~~landscape, the emission map shows the distribution of land cover (500m), we utilize the~~ NO_x fluxes ~~at the spatial resolution of~~
305 ~~the emission inventory, 4 km to yield an estimate of~~ NO_x emission at 4km. For each 4 km grid, we collect the observed fluxes whose 90% of the footprint overlaps with this grid area and define the weight r_k as the fractional area that the footprint covers. The emission, in a unit of mg N m⁻² h⁻¹, is calculated by the weighted average of flux (Eqn. 18). Only grids measured by at least five flux observations are considered in order to focus our attention on those pixels for which we have a statistically representative sample of the emissions.

$$310 \quad Emis_i = \frac{\sum_{k=1}^{n \geq 5} r_k F_k}{\sum_{k=1}^{n \geq 5} r_k} \quad (18)$$

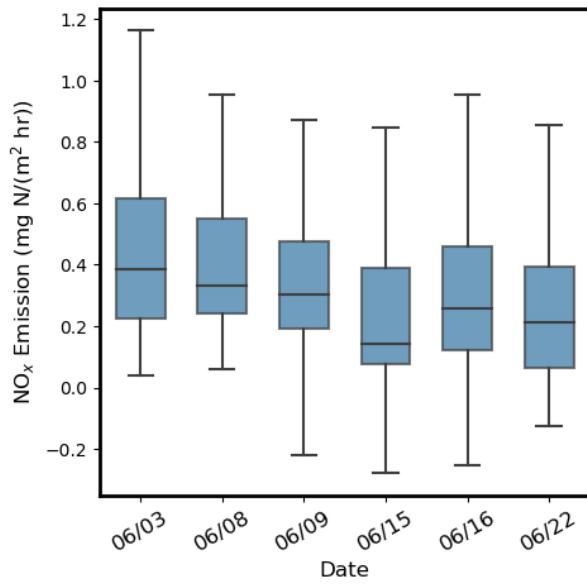
The emission is calculated based on the observations from ~~each flight six flights during weekdays~~(Fig. 6 (a)). ~~During RECAP-CA, we made six flights during weekdays.~~The largest reported weekday emission was on June 03 when the median emission was ~~1.07 mg~~0.39 mg N m⁻² h⁻¹. The lowest weekday emission was observed on June 15 with the median emission of ~~0.39 mg~~0.14 mg N m⁻² h⁻¹. The large daily variation observed in estimated emissions during weekdays is partially due to the variation in flight routes and footprint coverage. This is illustrated by the daily estimated emission map shown in Fig. S10. ~~We also made one weekend flight on June 13, and it yields estimated emissions that are significantly lower than the estimated emission on any weekday, which we attribute to reduced diesel truck activity at the weekend.~~

As the emission inventories make a distinction between weekdays and weekends and do not account for the daily variation on different weekdays, we average over the six-weekday flights to yield the best estimate of emission maps over the San Joaquin
320 Valley derived from flux measurements (Fig. 6 (b)). The median estimated weekday NO_x emission over the study domain is ~~0.70 mg~~0.26 mg N m⁻² h⁻¹ with the interquartile range of ~~0.40 and 1.34 mg~~0.14 and 0.46 mg N m⁻² h⁻¹. The observed emission map describes high NO_x emissions in the cities of Bakersfield (119°W, 35.3°N) and Fresno (119.8°W, 36.75°N) and along highway 99.

5.1 Evaluation of anthropogenic NO_x emission inventories

325 First, we compare the observations to the inventory developed by the California Air Resources Board (CARB). The anthropogenic emissions of NO_x consist of mobile sources, stationary sources, and other NO_x emissions from miscellaneous processes such as residential fuel combustion and managed disposal. In the CARB inventory, the mobile sources are estimated from Emission FACTor (EMFAC) v1.0.2 (CARB, 2021a) and OFFROAD mobile source emission models (CARB, 2021b). The stationary sources are estimated based on the reported survey of facilities within each local jurisdiction and the emission factors
330 from California Air Toxics Emission Factor (CATEF) database (CARB, 2021c). Hereinafter we utilize “EMFAC” to represent anthropogenic vehicle-related NO_x emissions used in the CARB inventory. An alternative anthropogenic emission inventory

(a)



(b)

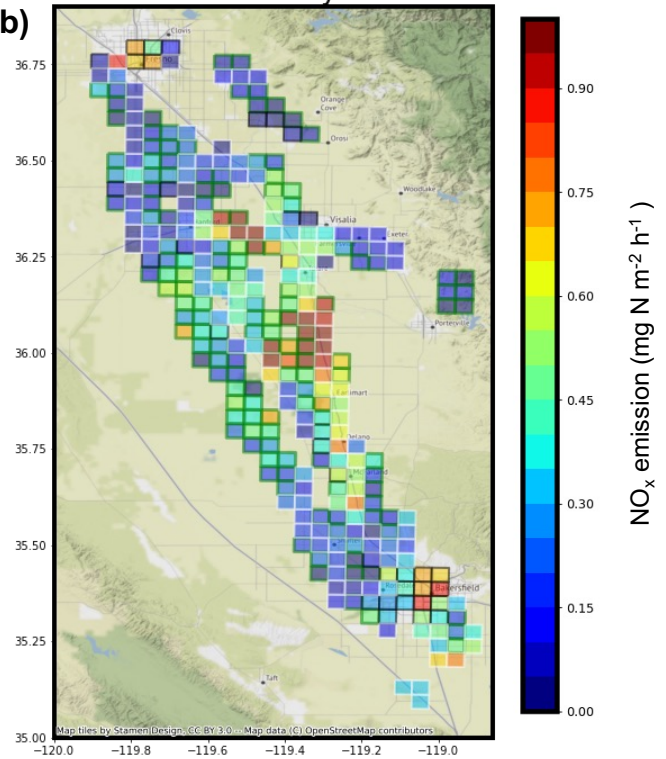


Figure 6. a) The whisker box plot of observed emissions for each flight, aligned in the order of flight days. The box represents the interquartile ranges of observed emissions and the line represents the median emission. The whiskers show the maximum and minimum values. ~~The weekdays are shown in blue and one weekend day is shown in red.~~ b) The spatial distribution of emission at 4 km over SJV derived from observed fluxes during weekdays. The patch color shows the observed NO_x emission. The edge color denotes the land cover type; the grid cells covering highways in white, those covering urban regions in black, and the rest of the grid cells that are categorized with cultivated soil land cover types in green. ©OpenStreetMap contributors 2022. Distributed under the Open Data Commons Open Database License (ODbL) v1.0.

is the fuel-based inventory for vehicle emissions (FIVE), developed by McDonald et al. (2012) and updated by Harkins et al. (2021). Both emission inventories are at 4 km spatial resolution.

To disentangle the contribution of different NO_x emissions sources, we attribute emissions at grid cells covering either highway or urban regions to anthropogenic emissions from transportation and fuel combustion, and those at remaining grid cells are categorized as soil NO_x emissions. For each grid cell categorized as anthropogenic emission dominant, we then match the emission inventories representing the weekday scenario to the same hour and grids of emissions derived from measured fluxes. The corresponding hour of this estimated emission is rounded to the closest hour of the observation times. Figure 7 ~~shows and Figure S12 show~~ the comparison of observed anthropogenic emissions against EMFAC and FIVE emission inventories. Over urban regions, the ~~mean and~~ median observed RECAP NO_x emission ~~is 1.10 mg~~ are 0.37 mg N m⁻² h⁻¹ and the interquartile range is ~~0.36 and 1.86 mg~~ 0.14 and 0.58 mg N m⁻² h⁻¹. Both EMFAC and FIVE yield a good agreement with our measurements; the ~~mean urban~~ NO_x ~~emission are~~ 0.40 and 0.43 mg N m⁻² h⁻¹. ~~However, the~~ median urban NO_x emission in these inventories is 24% and 22% lower than the observation, respectively. The estimated NO_x emission on grid cells covering highways is more scattered. The median estimated NO_x emission is ~~0.68 mg~~ 0.24 mg N m⁻² h⁻¹. It is lower than on urban grid cells due to spatial averaging and the fact that most of the highway length is outside the urban regions. The distribution of observed RECAP NO_x emissions from the highway is right-skewed, characterized by an interquartile range of ~~0.41 and 1.42 mg~~ 0.14 and 0.47 mg N m⁻² h⁻¹. We also note that over ~~highway~~ Highway 99, the RECAP NO_x emission is a factor of 3 higher than average on grid cells near congestion, reflecting the variation of emission caused by real-time traffic conditions. Both EMFAC and FIVE provide lower NO_x emissions over highway grids, the median NO_x emissions are ~~28% and~~ 36% and 50% of those from the RECAP observations. The highway pixels include a land cover that is mostly non-highway; typically soil. If soil N emissions are substantially larger than in these inventories, it is possible that the measurements and bottom-up inventories for highways are in better agreement than indicated by the figure.

5.2 Evaluation of soil NO_x scheme

Soil NO_x ~~varies nonlinearly with meteorological conditions, soil conditions, and agricultural activities. emissions are determined~~ by biogeochemical processes including soil microbe-mediated nitrification and denitrification. Process-based biogeochemical models have been developed to mechanistically represent soil NO_x emissions by simulating nitrogen interactions in ecological systems, such as DeNitrification-DeComposition (DNDC) (Li et al., 1992, 1994; Guo et al., 2020) and DayCENT (Del Grosso et al., 2000; . However, these process-level models are not yet widely applied to chemical transport models, and the default model configuration uses empirical soil NO_x schemes. The Model of Emissions of Gases and Aerosols from Nature v3 (MEGAN) (Guenther et al., 2012) is the most commonly used scheme and is used to predict soil NO_x emissions in the CARB emission inventory. It is gridded at 4 km spatial scale and has hourly time steps. The ~~biogenic~~ Biogenic Emission Inventory System (BEIS) is the default scheme to estimate volatile organic compounds from vegetation and NO from soil developed by the United States Environmental Protection Agency (EPA). We obtain the hourly BEIS v2.14 soil NO_x emission at 4 km during the study period from the Weather Research and Forecasting-Chemistry model (WRF-Chem) with the same model configuration described in Kim et al. (2022). ~~The~~ While soil NO_x varies nonlinearly with meteorological conditions, soil conditions, and agricultural activities, both

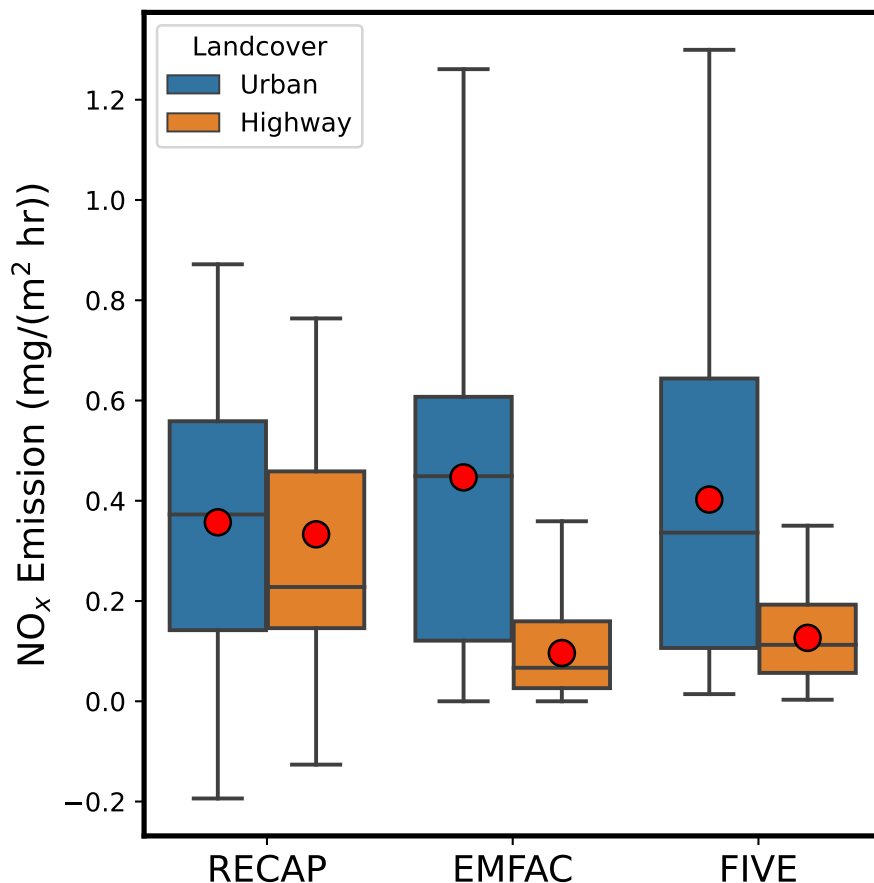


Figure 7. Whisker box plot of observed RECAP anthropogenic NO_x emissions from transportation and fuel combustion as well as those from EMFAC and FIVE emission inventories, separated by highway and urban land cover types. The box is the interquartile range with the line of the median value. The maximum and minimum emissions are shown by whiskers and the mean emissions are shown in red dots.

MEGAN and BEIS simplify the nonlinearity to an activity factor (γ), as a function of ambient temperature, leaf area index, and leaf age. A recently developed soil NO_x scheme, the Berkeley Dalhousie Iowa Soil NO Parameterization (BDISNP) (Hudman et al., 2012; Sha et al., 2021) is also used in a number of models. This parameterization, is an intermediate complexity model and includes more details than the other two in order to be more faithful to direct measurements made at soils and to describe their seasonal and hourly variations. The BDISNP includes parameters representing the effects of soil moisture, temperature, and soil nitrogen including fertilizer. Using the same WRF-Chem setup described in Sha et al. (2021), we also calculate the BDISNP soil NO_x emissions during the study period at the spatial resolution of 2 km and re-grid them to 4 km.

370

Figure. 8 (a) illustrates the range of soil N emissions derived from RECAP observations as compared to these three different soil NO_x schemes. The analysis of the observations exhibits a median cultivated soil NO_x emission of ~~0.68 mg~~ 0.26 mg N

375 $\text{m}^{-2} \text{h}^{-1}$ with a wide spread. The interquartile range of the inferred emission is $0.41\text{-}0.14 \text{ mg N m}^{-2} \text{h}^{-1}$ and $1.22\text{-}0.45 \text{ mg N m}^{-2} \text{h}^{-1}$. MEGAN and BEIS both have an order of magnitude lower emissions with median soil NO_x emissions of $0.018\text{-}0.023\text{-}0.008\text{-}0.011 \text{ mg N m}^{-2} \text{h}^{-1}$, respectively. The BDISNP soil NO_x scheme shows a median soil NO_x emission of $0.32\text{-}0.14 \text{ mg N m}^{-2} \text{h}^{-1}$. Figure. 8 (b) exhibits a point-by-point comparison of the observed RECAP and the
380 the observations. Figure S13 (a) and (d) shows the spatial distribution of soil NO_x emissions from observation and BDISNP scheme. Both show higher soil NO_x emissions between 35.75°N and 36.25°N .

A distinct characteristic of soil NO_x emission is its temperature dependence. For instance, Oikawa et al. (2015) identified unusually high soil NO_x emissions in a high-temperature agricultural region based on in-situ observations. The temperature-driven increase in soil NO_x emission raises concerns in the future warmer climate, resulting in a larger contribution to O_3
385 pollution (Romer et al., 2018). Here we leverage our flux observations to probe this temperature dependence. We collect observed NO_x emissions for each flight and select the subset of NO_x emissions on grids categorized as cultivated soil land type. We also collect corresponding mean soil temperature from WRF-Chem and match them to observed NO_x emissions both in time and space. A large variation range of soil temperature is observed, ranging from 292K between 295K to 304K is observed. We then bin observed soil NO_x emissions to three soil temperature categories, each of which has 4K intervals.
390 The median soil NO_x emissions increase from $0.51\text{-}0.22 \text{ mg N m}^{-2} \text{h}^{-1}$ to $0.77\text{-}0.29 \text{ mg N m}^{-2} \text{h}^{-1}$ with the mean median soil temperature increasing from 294K to $302\text{-}296\text{K}$ to 300K . As the response to soil temperature is incorporated in the BDISNP scheme, we also bin the BDISNP parameterized soil NO_x emissions into the same soil temperature categories. Both the RECAP measured flux and the BDISNP modeled soil NO_x emissions exhibit an approximately 33% increase over the range of soil temperature shown.

395 5.3 Discussion of soil NO_x emissions

Soil NO_x emissions in California have been studied in field experiments. Matson et al. (1997) measured soil NO_x emissions from nine dominant crop types in SJV and reported mean fluxes of $0.01\text{-}0.09 \text{ mg N m}^{-2} \text{h}^{-1}$. They also reported a large variation of measured NO_x flux among crops and among different fields of the same crop; the highest measured NO_x flux is $0.17 \text{ mg N m}^{-2} \text{h}^{-1}$ due to the fertilizer application and soil moisture characteristics. Horwath and Burger (2013) observed
400 an average flux of $0.05\text{-}0.28 \text{ mg N m}^{-2} \text{h}^{-1}$ at mid-days during summertime from five crops in California, and the highest NO_x flux is $>4 \text{ mg N m}^{-2} \text{h}^{-1}$ in systems receiving large N inputs resulting in high concentrations of ammonium. Oikawa et al. (2015) observed soil NO_x emissions in a high-temperature fertilized agricultural region of the Imperial Valley, CA, ranging between -0.02 and $3.2 \text{ mg N m}^{-2} \text{h}^{-1}$. They also conducted control experiments to investigate the soil NO_x emission responses to fertilization and irrigation. The highest soil NO_x flux was reported ~ 10 days after the fertilizer at the soil volumetric water
405 content of 30% and the soil temperature of $\sim 313\text{K}$.

The mean soil NO_x flux, $0.32 \text{ mg N m}^{-2} \text{h}^{-1}$, derived in our flux measurements is higher than the mean fluxes reported in Matson et al. (1997) and Horwath and Burger (2013), however, the range of estimated soil NO_x flux is within those in Horwath and Burger (2013) and Oikawa et al. (2015). Fertilizer is likely the primary contributor to the higher mean soil NO_x .

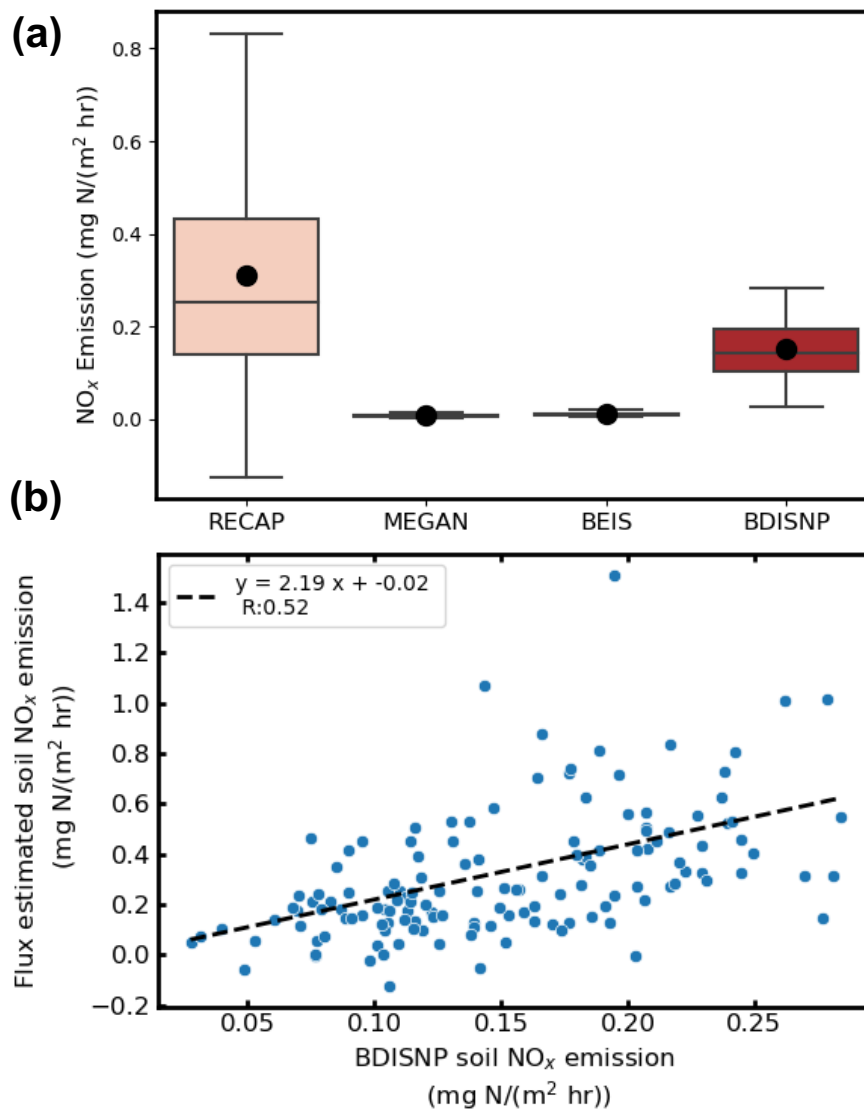


Figure 8. a) The whisker box plot of observed soil NO_x emissions and parameterized soil NO_x emissions from MEGAN, BEIS and BDISNP schemes. The mean soil NO_x emissions are shown in black dots. b) The scatter plot of soil NO_x emissions calculated from BDISNP scheme and from flux measurements. The dashed black is the least-square linear fit.

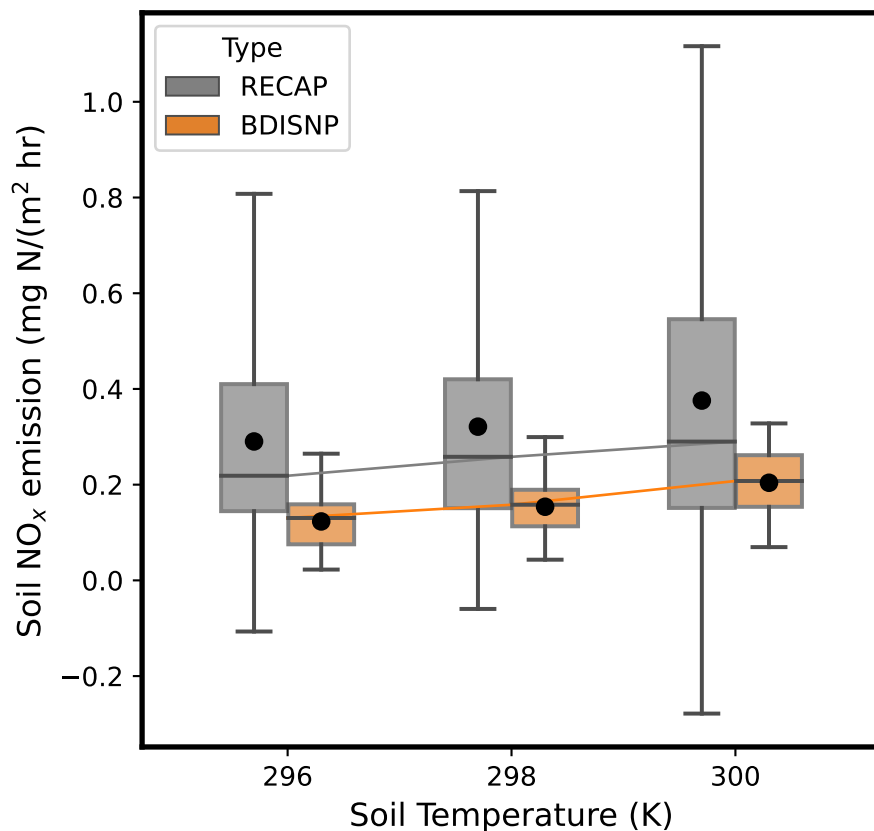


Figure 9. The dependence of soil NO_x emissions on soil temperature from both flux measurements (gray) and BDISNP scheme (orange). Both observed and BDISNP soil NO_x emissions are binned based on mean soil temperature from WRF-Chem. Three soil temperature bins are described with 4k intervals. The whisker box shows the distribution and the black dot shows the mean within each bin and the line connects median soil NO_x emissions across three bins.

410 flux in our study. The RECAP-CA field campaign was conducted in June, right after the month of peak fertilizer use in SJV (Guo et al., 2020). Shown in Oikawa et al. (2015), soil NO_x flux can increase up to 5-fold within 20 days of fertilizer. The higher mean soil NO_x flux is also contributed by higher soil temperature. In our study, the mean soil temperature is 299K with a range between 295K and 304K, whereas the observations in Horwath and Burger (2013) and Oikawa et al. (2015) spread over a wider range of soil temperature, 288K-315K. Consistent with our study, the temperature dependence of soil NO_x emission is observed in these field experiments. Horwath and Burger (2013) reported a 2.5-3.5 fold increase in NO_x fluxes with 10-degree
 415 increase in soil temperature. Oikawa et al. (2015) showed that the temperature dependence of soil NO_x emission is non-linear; a steeper increase in soil NO_x emission was observed with the soil temperature exceeding 295K.

It is worth noting the limitation of estimated soil NO_x emissions in our study. First of all, we are unable to investigate the dependence of soil NO_x emissions on meteorological drivers other than soil temperature, such as soil moisture, as modeled soil

moisture presents very small variation during the field campaign. Second, as our measurements only cover limited cropland areas in SJV over a short time period and it is around the time of fertilizer use, we cannot scale the estimated soil NO_x emission to the whole year or to the total cropland areas in California. Last, in the absence of ozone and PM2.5 observations, we cannot investigate the impact of soil NO_x emission on air quality. However, as the SJV is in the NO_x limited regime (Pusede et al., 2014), we expect a model that captures the soil NO_x more accurately will produce higher ozone. Future work is needed to further advance our understanding of soil NO_x emission and its role in urban and rural air pollution.

425 6 Conclusions

We performed airborne NO_x flux measurements during RECAP-CA field campaign over the San Joaquin Valley. Seven flights were made over the SJV in June 2021. When combined with footprint and land cover information, we resolve spatial heterogeneity in landscape flux. The component fluxes are estimated based on the multi-linear regression and exhibit statistically significant differences. The component fluxes are the highest from highways at ~~2.95 mg~~ 0.96 mg N m⁻² h⁻¹. Cultivated soil land types emit a non-negligible flux of ~~0.79 mg~~ 0.30 mg N m⁻² h⁻¹. The airborne flux observations are projected to a 4 km grid spacing to yield an estimated emission map over the SJV. We utilize this map to evaluate emission inventories commonly used in photochemical modeling. The anthropogenic emission inventories, EMFAC and FIVE, agree ~~with estimated~~ well with estimated mean NO_x emissions over urban regions ~~within 27% and 24%, respectively~~. However, the widely used, but not ~~state-of-the-science~~ biogeochemical process-based, models for soil NO_x emissions underestimate emissions by an order of magnitude or more in the SJV, leading to a poor assessment of the relative roles of mobile and agriculture sources of NO_x in the region. The BDISNP model as adapted by Sha et al. (2021) results in a better comparison with the observations. Even though it is still lower by a factor of ~~2.72~~, we show it yields a similar spatial pattern and soil temperature dependence as observed. Variations of this model are embedded in CMAQ (Rasool et al., 2019) and GEOS-CHEM (Wang et al., 2021) and have been implemented in WRF-CHEM by (Sha et al., 2021). Studies, where soil NO_x is potentially important, should make use of these codes, all of which are more consistent with observations at multiple scales.

Code and data availability. The measurement data from the RECAP field campaign is available at <https://csl.noaa.gov/projects/sunvex/>. The analysis codes for this study are available at <https://github.com/qdzh/FLUX/>.

Author contributions. RCC and AHG supervised the research; BP, EP, BS, PW, CA, AB, JS, RCC, AHG participated in the field campaign; BP and PW conducted the NO_x measurements; ST, HZ and JW provided model simulated BDISNP soil NO_x emissions; QZ performed the analysis with contributions from BP, EP, CN; QZ prepared the manuscript; all authors have reviewed and edited the paper.

Competing interests. The authors have the following competing interests: At least one of the (co-)authors is a member of the editorial board of Atmospheric Chemistry and Physics.

Acknowledgements. This RECAP field campaign was funded by California Air Resources Board Contract number 20RD003, 20AQP012, and Presidential Early Career Award for Scientists and Engineers (PECASE) (from Brian McDonald). QZ was supported by NOAA Climate & Global Change Postdoc Fellowship and EP was supported by a Feodor Lynen Fellowship of the Alexander von Humboldt Foundation. [JW and HZ acknowledge the support of NASA Atmospheric Composition and Modeling Program \(ACMAP, grant : 80NSSC19K0950\)](#) We thank Dennis Baldocchi, Glenn Wolfe, Erin Delaria for their help in calculating vertical divergence, and Brian McDonald, Rebecca Schwantes, Siyuan Wang for engaging in discussions at project meetings. We appreciate use of the emission inventories provided by Modeling and Meteorology Branch at CARB and NOAA Chemical Sciences Laboratory. We acknowledge the help from pilots, Bryce Kujat and George Loudakis, during the RECAP field campaign.

References

- Almaraz, M., Bai, E., Wang, C., Trousdell, J., Conley, S., Faloona, I., and Houlton, B. Z.: Agriculture is a major source of NO_x pollution in California, *Science advances*, 4, eaao3477, 2018.
- American Lung Association: State of the Air Report, <https://www.lung.org/research/sota>, last accessed on 06/22/2022, 2020.
- 460 Andreae, M. O. and Schimel, D. S.: Exchange of trace gases between terrestrial ecosystems and the atmosphere, 1990.
- CARB: Heavy-Duty Engine and Vehicle Omnibus Regulation and Associated Amendments, <https://ww2.arb.ca.gov/rulemaking/2020/hdomnibuslownox>, last accessed on 06/22/2022, 2016.
- CARB: Emission FACTor (EMFAC), <https://arb.ca.gov/emfac/>, last accessed on 06/22/2022, 2021a.
- CARB: OFFROAD2021 model, <https://ww2.arb.ca.gov/our-work/programs/mobile-source-emissions-inventory/msei-road-documentation-0>, last accessed on 06/22/2022, 2021b.
- 465 CARB: Stationary Emissions by Air District, <https://ww2.arb.ca.gov/applications/emissions-air-district>, last accessed on 06/22/2022, 2021c.
- Day, D., Wooldridge, P., Dillon, M., Thornton, J., and Cohen, R.: A thermal dissociation laser-induced fluorescence instrument for in situ detection of NO₂, peroxy nitrates, alkyl nitrates, and HNO₃, *Journal of Geophysical Research: Atmospheres*, 107, ACH-4, 2002.
- De Gouw, J. A., Parrish, D. D., Frost, G. J., and Trainer, M.: Reduced emissions of CO₂, NO_x, and SO₂ from US power plants owing to
- 470 switch from coal to natural gas with combined cycle technology, *Earth's Future*, 2, 75–82, 2014.
- Del Grosso, S., Parton, W., Mosier, A., Ojima, D., Kulmala, A., and Phongpan, S.: General model for N₂O and N₂ gas emissions from soils due to denitrification, *Global biogeochemical cycles*, 14, 1045–1060, 2000.
- Drysdale, W. S., Vaughan, A. R., Squires, F. A., Cliff, S. J., Metzger, S., Durden, D., Pinguha-Durden, N., Helfter, C., Nemitz, E., Grimmond, C. S. B., et al.: Eddy Covariance Measurements Highlight Sources of Nitrogen Oxide Emissions Missing from Inventories for Central
- 475 London, *Atmospheric Chemistry and Physics Discussions*, pp. 1–35, 2022.
- EPA: Air Pollutant Emissions Trends Data, <https://www.epa.gov/air-emissions-inventories/air-pollutant-emissions-trends-data>, last accessed on 10/28/2021, 2016.
- Gu, D., Guenther, A. B., Shilling, J. E., Yu, H., Huang, M., Zhao, C., Yang, Q., Martin, S. T., Artaxo, P., Kim, S., et al.: Airborne observations reveal elevational gradient in tropical forest isoprene emissions, *Nature communications*, 8, 1–7, 2017.
- 480 Guenther, A., Jiang, X., Heald, C. L., Sakulyanontvittaya, T., Duhl, T. a., Emmons, L., and Wang, X.: The Model of Emissions of Gases and Aerosols from Nature version 2.1 (MEGAN2. 1): an extended and updated framework for modeling biogenic emissions, *Geoscientific Model Development*, 5, 1471–1492, 2012.
- Guo, L., Chen, J., Luo, D., Liu, S., Lee, H. J., Motallebi, N., Fong, A., Deng, J., Rasool, Q. Z., Avise, J. C., et al.: Assessment of nitrogen oxide emissions and San Joaquin Valley PM_{2.5} impacts from soils in California, *Journal of Geophysical Research: Atmospheres*, 125, e2020JD033304, 2020.
- 485 Hakeem, K. R., Sabir, M., Ozturk, M., Akhtar, M., Ibrahim, F. H., et al.: Nitrate and nitrogen oxides: sources, health effects and their remediation, *Reviews of Environmental Contamination and Toxicology Volume 242*, pp. 183–217, 2016.
- Hannun, R. A., Wolfe, G. M., Kawa, S. R., Hanisco, T. F., Newman, P. A., Alfieri, J. G., Barrick, J., Clark, K. L., DiGangi, J. P., Diskin, G. S., et al.: Spatial heterogeneity in CO₂, CH₄, and energy fluxes: Insights from airborne eddy covariance measurements over the Mid-Atlantic region, *Environmental Research Letters*, 15, 035008, 2020.
- 490 Harkins, C., McDonald, B. C., Henze, D. K., and Wiedinmyer, C.: A fuel-based method for updating mobile source emissions during the COVID-19 pandemic, *Environmental Research Letters*, 16, 065018, 2021.

- Högström, U.: Non-dimensional wind and temperature profiles in the atmospheric surface layer: A re-evaluation, in: *Topics in Micrometeorology*. A Festschrift for Arch Dyer, pp. 55–78, Springer, 1988.
- 495 Horwath, W. R. and Burger, M.: Assessment of NO_x Emissions from Soil in California Cropping Systems, Tech. Rep. Contract No. 09–329, California Environmental Protection Agency, Air Resources Board, Sacramento, CA, 2013.
- Hudman, R., Moore, N., Mebust, A., Martin, R., Russell, A., Valin, L., and Cohen, R.: Steps towards a mechanistic model of global soil nitric oxide emissions: implementation and space based-constraints, *Atmospheric Chemistry and Physics*, 12, 7779–7795, 2012.
- Hutjes, R., Vellinga, O., Gioli, B., and Miglietta, F.: Dis-aggregation of airborne flux measurements using footprint analysis, *Agricultural and Forest Meteorology*, 150, 966–983, 2010.
- 500 Kampa, M. and Castanas, E.: Human health effects of air pollution, *Environmental pollution*, 151, 362–367, 2008.
- Karl, T., Apel, E., Hodzic, A., Riemer, D., Blake, D., and Wiedinmyer, C.: Emissions of volatile organic compounds inferred from airborne flux measurements over a megacity, *Atmospheric Chemistry and Physics*, 9, 271–285, 2009.
- Karl, T., Misztal, P., Jonsson, H., Shertz, S., Goldstein, A., and Guenther, A.: Airborne flux measurements of BVOCs above Californian oak forests: Experimental investigation of surface and entrainment fluxes, OH densities, and Damköhler numbers, *Journal of the atmospheric sciences*, 70, 3277–3287, 2013.
- 505 Kaser, L., Karl, T., Yuan, B., Mauldin III, R., Cantrell, C., Guenther, A. B., Patton, E., Weinheimer, A. J., Knote, C., Orlando, J., et al.: Chemistry-turbulence interactions and mesoscale variability influence the cleansing efficiency of the atmosphere, *Geophysical Research Letters*, 42, 10–894, 2015.
- 510 Kim, S.-W., McDonald, B. C., Seo, S., Kim, K.-M., and Trainer, M.: Understanding the paths of surface ozone abatement in the Los Angeles Basin, *Journal of Geophysical Research: Atmospheres*, 127, e2021JD035 606, 2022.
- Kljun, N., Calanca, P., Rotach, M., and Schmid, H.: A simple parameterisation for flux footprint predictions, *Boundary-Layer Meteorology*, 112, 503–523, 2004.
- Langford, B., Acton, W., Ammann, C., Valach, A., and Nemitz, E.: Eddy-covariance data with low signal-to-noise ratio: time-lag determination, uncertainties and limit of detection, *Atmospheric Measurement Techniques*, 8, 4197–4213, 2015.
- 515 Lelieveld, J., Evans, J. S., Fnais, M., Giannadaki, D., and Pozzer, A.: The contribution of outdoor air pollution sources to premature mortality on a global scale, *Nature*, 525, 367–371, 2015.
- Lenschow, D., Mann, J., and Kristensen, L.: How long is long enough when measuring fluxes and other turbulence statistics?, *Journal of Atmospheric and Oceanic Technology*, 11, 661–673, 1994.
- 520 Li, C., Frolking, S., and Frolking, T. A.: A model of nitrous oxide evolution from soil driven by rainfall events: 1. Model structure and sensitivity, *Journal of Geophysical Research: Atmospheres*, 97, 9759–9776, 1992.
- Li, C., Frolking, S., and Harriss, R.: Modeling carbon biogeochemistry in agricultural soils, *Global biogeochemical cycles*, 8, 237–254, 1994.
- Matson, P., Firestone, M., Herman, D., Billow, T., Kiang, N., Benning, T., and Burns, J.: *Agricultural Systems in the San Joaquin Valley: Development of Emissions Estimates for Nitrogen Oxides*, Tech. Rep. Contract No. 94–732, California Environmental Protection Agency, Air Resources Board, Sacramento, CA, 1997.
- 525 Mauder, M., Desjardins, R. L., and MacPherson, I.: Scale analysis of airborne flux measurements over heterogeneous terrain in a boreal ecosystem, *Journal of Geophysical Research: Atmospheres*, 112, 2007.
- McDonald, B. C., Dallmann, T. R., Martin, E. W., and Harley, R. A.: Long-term trends in nitrogen oxide emissions from motor vehicles at national, state, and air basin scales, *Journal of Geophysical Research: Atmospheres*, 117, 2012.

- 530 Metzger, S., Junkermann, W., Mauder, M., Beyrich, F., Butterbach-Bahl, K., Schmid, H.-P., and Foken, T.: Eddy-covariance flux measurements with a weight-shift microlight aircraft, *Atmospheric Measurement Techniques*, 5, 1699–1717, 2012.
- Misztal, P., Karl, T., Weber, R., Jonsson, H., Guenther, A. B., and Goldstein, A. H.: Airborne flux measurements of biogenic isoprene over California, *Atmospheric Chemistry and Physics*, 14, 10631–10647, 2014.
- Nussbaumer, C. M., Place, B. K., Zhu, Q., Pfannerstill, E. Y., Wooldridge, P., Schulze, B. C., Arata, C., Ward, R., Bucholtz, A., Seinfeld, J. H., Goldstein, A. H., and Cohen, R. C.: Measurement report: Airborne measurements of NO_x fluxes over Los Angeles during the RECAP-CA 2021 campaign, *EGUsphere*, 2023, 1–20, <https://doi.org/10.5194/egusphere-2023-601>, 2023.
- 535 Oikawa, P., Ge, C., Wang, J., Eberwein, J., Liang, L., Allsman, L., Grantz, D., and Jenerette, G.: Unusually high soil nitrogen oxide emissions influence air quality in a high-temperature agricultural region, *Nature communications*, 6, 1–10, 2015.
- Pfannerstill, E. Y., Arata, C., Zhu, Q., Schulze, B. C., Woods, R., Seinfeld, J. H., Bucholtz, A., Cohen, R. C., and Goldstein, A. H.: Volatile organic compound fluxes in the San Joaquin Valley – spatial distribution, source attribution, and inventory comparison, *EGUsphere*, 2023, 1–42, <https://doi.org/10.5194/egusphere-2023-723>, 2023.
- 540 Phoenix, G. K., Hicks, W. K., Cinderby, S., Kuylenstierna, J. C., Stock, W. D., Dentener, F. J., Giller, K. E., Austin, A. T., Lefroy, R. D., Gimeno, B. S., et al.: Atmospheric nitrogen deposition in world biodiversity hotspots: the need for a greater global perspective in assessing N deposition impacts, *Global Change Biology*, 12, 470–476, 2006.
- 545 Pusede, S., Gentner, D., Wooldridge, P., Browne, E., Rollins, A., Min, K.-E., Russell, A., Thomas, J., Zhang, L., Brune, W., et al.: On the temperature dependence of organic reactivity, nitrogen oxides, ozone production, and the impact of emission controls in San Joaquin Valley, California, *Atmospheric Chemistry and Physics*, 14, 3373–3395, 2014.
- Rasool, Q. Z., Bash, J. O., and Cohan, D. S.: Mechanistic representation of soil nitrogen emissions in the Community Multiscale Air Quality (CMAQ) model v 5.1, *Geoscientific Model Development*, 12, 849–878, 2019.
- 550 Romer, P. S., Duffey, K. C., Wooldridge, P. J., Edgerton, E., Baumann, K., Feiner, P. A., Miller, D. O., Brune, W. H., Koss, A. R., De Gouw, J. A., et al.: Effects of temperature-dependent NO_x emissions on continental ozone production, *Atmospheric Chemistry and Physics*, 18, 2601–2614, 2018.
- Sayres, D. S., Dobosy, R., Healy, C., Dumas, E., Kochendorfer, J., Munster, J., Wilkerson, J., Baker, B., and Anderson, J. G.: Arctic regional methane fluxes by ecotope as derived using eddy covariance from a low-flying aircraft, *Atmospheric Chemistry and Physics*, 17, 8619–8633, 2017.
- 555 Schaller, C., Göckede, M., and Foken, T.: Flux calculation of short turbulent events—comparison of three methods, *Atmospheric Measurement Techniques*, 10, 869–880, 2017.
- Sha, T., Ma, X., Zhang, H., Janecek, N., Wang, Y., Wang, Y., Castro Garcí'a, L., Jenerette, G. D., and Wang, J.: Impacts of Soil NO_x Emission on O₃ Air Quality in Rural California, *Environmental science & technology*, 55, 7113–7122, 2021.
- 560 Sührling, M., Metzger, S., Xu, K., Durden, D., and Desai, A.: Trade-offs in flux disaggregation: a large-eddy simulation study, *Boundary-Layer Meteorology*, 170, 69–93, 2019.
- Thornton, J. A., Wooldridge, P. J., and Cohen, R. C.: Atmospheric NO₂: In situ laser-induced fluorescence detection at parts per trillion mixing ratios, *Analytical Chemistry*, 72, 528–539, 2000.
- Torrence, C. and Compo, G. P.: A practical guide to wavelet analysis, *Bulletin of the American Meteorological society*, 79, 61–78, 1998.
- 565 Tsai, J.-H., Huang, P.-H., and Chiang, H.-L.: Characteristics of volatile organic compounds from motorcycle exhaust emission during real-world driving, *Atmospheric Environment*, 99, 215–226, 2014.

- Vaughan, A. R., Lee, J. D., Misztal, P. K., Metzger, S., Shaw, M. D., Lewis, A. C., Purvis, R. M., Carslaw, D. C., Goldstein, A. H., Hewitt, C. N., et al.: Spatially resolved flux measurements of NO_x from London suggest significantly higher emissions than predicted by inventories, *Faraday discussions*, 189, 455–472, 2016.
- 570 Vaughan, A. R., Lee, J. D., Metzger, S., Durden, D., Lewis, A. C., Shaw, M. D., Drysdale, W. S., Purvis, R. M., Davison, B., and Hewitt, C. N.: Spatially and temporally resolved measurements of NO_x fluxes by airborne eddy covariance over Greater London, *Atmospheric Chemistry and Physics*, 21, 15 283–15 298, 2021.
- Wang, Y., Ge, C., Garcia, L. C., Jenerette, G. D., Oikawa, P. Y., and Wang, J.: Improved modelling of soil NO_x emissions in a high temperature agricultural region: role of background emissions on NO₂ trend over the US, *Environmental research letters*, 16, 084 061, 575 2021.
- Wolfe, G., Hanisco, T., Arkinson, H., Bui, T., Crounse, J., Dean-Day, J., Goldstein, A., Guenther, A., Hall, S., Huey, G., et al.: Quantifying sources and sinks of reactive gases in the lower atmosphere using airborne flux observations, *Geophysical Research Letters*, 42, 8231–8240, 2015.
- Wolfe, G. M., Kawa, S. R., Hanisco, T. F., Hannun, R. A., Newman, P. A., Swanson, A., Bailey, S., Barrick, J., Thornhill, K. L., Diskin, G., 580 et al.: The NASA carbon airborne flux experiment (CARAFE): instrumentation and methodology, *Atmospheric Measurement Techniques*, 11, 1757–1776, 2018.
- Wooldridge, P., Perring, A., Bertram, T., Flocke, F., Roberts, J., Singh, H., Huey, L., Thornton, J., Wolfe, G., Murphy, J., et al.: Total Peroxy Nitrates (Σ PNs) in the atmosphere: the Thermal Dissociation-Laser Induced Fluorescence (TD-LIF) technique and comparisons to speciated PAN measurements, *Atmospheric Measurement Techniques*, 3, 593–607, 2010.
- 585 Yu, H., Guenther, A., Gu, D., Warneke, C., Geron, C., Goldstein, A., Graus, M., Karl, T., Kaser, L., Misztal, P., et al.: Airborne measurements of isoprene and monoterpene emissions from southeastern US forests, *Science of the Total Environment*, 595, 149–158, 2017.
- Yuan, B., Kaser, L., Karl, T., Graus, M., Peischl, J., Campos, T. L., Shertz, S., Apel, E. C., Hornbrook, R. S., Hills, A., et al.: Airborne flux measurements of methane and volatile organic compounds over the Haynesville and Marcellus shale gas production regions, *Journal of Geophysical Research: Atmospheres*, 120, 6271–6289, 2015.